Regular Article

On the potential energy landscape of supercooled liquids and glasses

D. Rodney[1,a] and T. Schrøder[2]

[1] Laboratoire Science et Ingénierie des Matériaux et Procédés, Grenoble INP, UJF, CNRS, Domaine Universitaire BP 46, F38402 Saint Martin d'Hères, France
[2] Department of Sciences, DNRF Centre "Glass and Time", IMFUFA, Roskilde University, P.O. Box 260, DK-4000 Roskilde, Denmark

Abstract. The activation-relaxation technique (ART), a saddle-point search method, is applied to determine the potential energy landscape around supercooled and glassy configurations of a three-dimensional binary Lennard-Jones system. We show a strong relation between the distribution of activation energies around a given glassy configuration and its history, in particular, the cooling rate used to produce the glass and whether or not the glass was plastically deformed prior to sampling. We also compare the thermally activated transitions found by ART around a supercooled configuration with the succession of transitions undergone by the same supercooled liquid during a time trajectory simulated by molecular dynamics. We find that ART is biased towards more heterogeneous transitions with higher activation energies and more broken bonds than the MD simulation.

1 Introduction

Understanding the glass transition is a field of intense research (see, for example, [1–6]), which has greatly benefited from the recognition that the dynamics of a cooling liquid is intimately related to the topography of its potential energy landscape (PEL). Probably, the most useful approach is based on molecular dynamics (MD) simulations with regular potential energy minimizations to track the succession of energy basins, or inherent structures (ISs), visited by the liquid during its time trajectory, either during cooling towards the glass transition [7–10] or at constant temperature near and above the mode coupling temperature, T_C [11–13]. We know from these studies that the rapid slowing down and stretched exponential relaxations of liquids across the glass transition [13,4] are due to the multifunnel rough structure of the PEL [14] with a hierarchy of energy barriers connecting basins and metabasins, in which the liquid gets progressively trapped during cooling.

Equilibrium MD simulations can only be used above T_C (or slightly below) because below this temperature, in the glassy regime, the dynamics of the system becomes thermally activated and very slow, that is at the limit or beyond the timescale accessible to direct MD simulations. In this regime, saddle-point search methods, for example the activation-relaxation technique (ART) [15–17], can be

used to sample locally the PEL around a glassy configuration and determine distributions of thermally activated paths leaving the configuration. In refs. [17,18], the effect of a plastic deformation and of ageing on such distribution was studied in the case of a two-dimensional binary Lennard-Jones (LJ) glass.

In the present paper, we extend the application of ART to three-dimensional glasses, using Wahnström potential [19], a very well-characterized binary LJ potential. We use ART to sample the PEL in three distinct conditions: glasses at different quench rates (sect. 3), plastically deformed glasses (sect. 4) and a supercooled liquid (sect. 5), with a comparison between the thermally activated transitions identified by ART and the transitions undergone by the same supercooled liquid during a time trajectory simulated by MD.

2 Methodology

Interatomic interactions are modeled using Wahnström binary LJ potential [19], a potential widely used to study liquids and glasses [11,20–22]. Throughout the paper, we will use LJ units: ϵ_{AA}, σ_{AA} and m_A for energy, length and mass, and $t_0 = \sigma_{AA}\sqrt{m_A/\epsilon_{AA}}$ for the time unit. The system is made of 10000 particles, 4971 A particles and 5029 B particles (with $\epsilon_{BB} = 1.0$ and $\sigma_{BB} = 5/6$, $m_B = 0.5$) and coupling parameters $\epsilon_{AB} = 1.0$, $\sigma_{AB} = 11/12$ and a cut-off radius at $2.5\sigma_{AA}$ with a simple energy
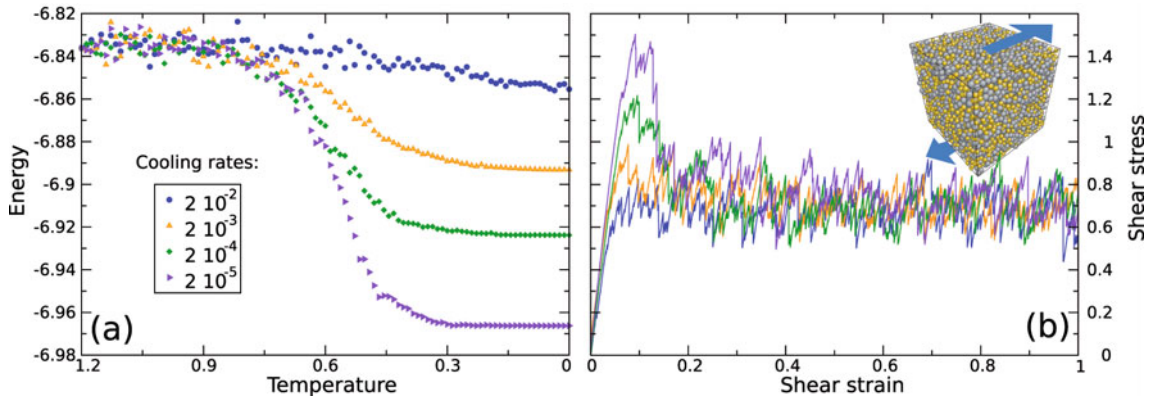
Fig. 1. (Colour on-line) Influence of the cooling rate on glass properties: (a) inherent structure potential energy as a function of temperature during cooling at various cooling rates noted in the figure (LJ units are used). (b) Shear stress/shear strain curves during quasistatic simple shear deformation of the glasses obtained in (a).

shift. The number density of the system is 1.296 with constant volume and periodic boundary conditions. The mode-coupling temperature, which plays the role of the glass transition temperature in atomistic simulations, is $0.59\epsilon_{AA}$ for this system [11]. The liquid is cooled using Andersen thermostat with a frequency of 10^{-3}. Energy minimizations to inherent structures are performed using a quenched dynamics algorithm [23]. Simple shear deformation is then applied quasistatically using Lees-Edwards shifted periodic boundary conditions and strain increments of 10^{-4}.

The MD trajectory of the supercooled liquid at $T_C = 0.59$ is taken from ref. [11], where the system is made of 500 particles with the same number density as the 10000 particle system.

To sample the first-order activated states around glassy configurations, we employ the activation-relaxation technique (ART), an eigenvector-following method in which the direction of minimum curvature is obtained iteratively using the Lanczos algorithm [15–17]. The methods starts with an activation phase where the initial equilibrium configuration is pushed out of its basin of attraction along a random direction in configuration space with a fixed step length of $0.025\sigma_{AA}$. The localized nature of thermal excitations is accounted for by choosing the initial direction as a random displacement of a randomly chosen atom. After the displacement, 5 relaxation steps are taken perpendicularly to the direction of motion to avoid a rapid rise of the system energy. This procedure is iterated until the curvature (*i.e.* the minimum eigenvalue of the Hessian matrix) becomes less than $-3.0\epsilon_{AA}/\sigma_{AA}^2$. A relaxation phase towards the saddle point is then started, by following the same procedure as above but using the variable step length proposed by Cancès *et al.* [16] with a maximum step length of $0.3\sigma_{AA}$. The saddle point is considered reached when the maximum atomic force component becomes less than $10^{-2}\epsilon_{AA}/\sigma_{AA}^2$. The saddle-point configuration is then perturbed along the unstable mode, both towards and away from the initial configuration, in order to ensure that the saddle point is connected to the initial configuration and to obtain the complete transition path, from the initial to the final configuration. The

activation energy is then just the energy difference between initial and activated configurations. The choice of the numerical parameters mentioned above (step lengths in activation and relaxation phases, threshold curvature, number of atoms involved in initial random direction of motion) is crucial for the efficiency of the method [17].

To identify the saddle point between the initial and final configurations during the MD trajectory, we used the nudged elastic band (NEB) method [24,25]. Within this method, an initial path is constructed between initial and final configurations by creating replicas of the system (20 of them) by linear interpolation between the two configurations. The replicas are linked between near neighbors in configuration space by linear springs of strength $0.1\epsilon_{AA}/\sigma_{AA}^2$. The energy of the path is minimized using a projected algorithm [24] whereby only the component of the force arising from the potential energy perpendicular to the path (which drives the system towards a minimum energy path) and that of the spring force parallel to the path (which keeps the replicas away from each other) are kept. We employed an improved tangent [26] and a climbing NEB procedure [27]. After the NEB calculation has converged, the highest energy configuration and local tangent to the minimum energy path were used in ART to determine with precision the saddle-point configuration of the transition.

3 PEL of quenched glasses

To produce glasses with different levels of relaxation, we cooled down liquids at different cooling rates, ranging from $2 \cdot 10^{-2}$ to $2 \cdot 10^{-5}$ in LJ units, with regular energy minimization to follow the succession of ISs visited by the system during its time evolution. The resulting IS energy curves are shown in fig. 1(a). As first reported by Sastry *et al.* [10] with a different interatomic potential, three dynamical regimes can be identified: i) the liquid regime at high temperatures where the IS potential energy is independent of cooling rate and temperature, ii) a regime where the IS potential energy is strongly dependent on both cooling rate and temperature, and iii) the
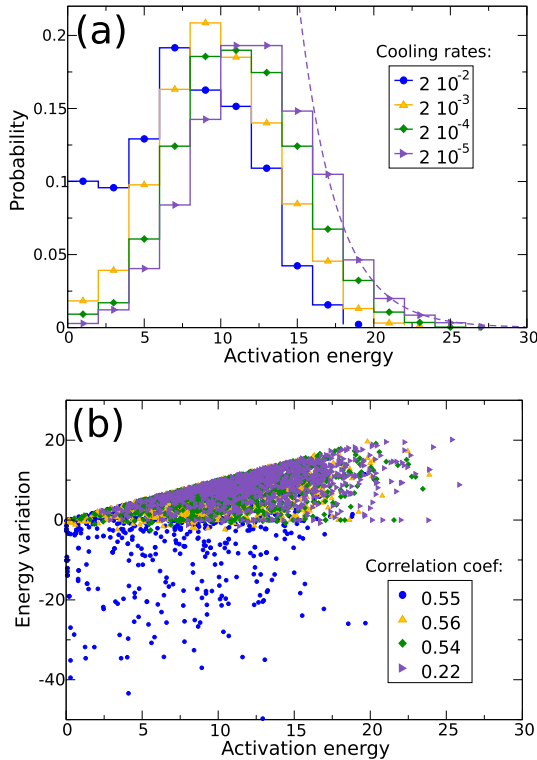
Fig. 2. (Colour on-line) Sampling of PEL with ART. (a) Probability distributions of activation energies in the glassy configurations obtained in fig. 1 at different quench rates. (b) Scatter plot of the energy difference between initial and final configurations as a function of the activation energy for 1000 transitions determined on the same configurations as in (a). The inset in (b) lists the correlation coefficient between activation energy and energy variation for the different data sets. The same color code applies as in fig. 1. The dashed curve in (a) is an exponential fit of the high-energy tail of the distribution with a cooling rate of $2 \cdot 10^{-5}$.

glassy regime where the IS potential energy only depends on cooling rate.

At low temperatures the dynamics of the liquid is well separated into vibrations around inherent states and thermally activated transitions between inherent states [28]. From MD simulations it was found that the temperature where this scenario becomes a good description is close to the estimated T_C [11]. In this regime, saddle-point search methods such as ART become useful because they allow to determine saddle-point configurations and potentially thermally activated transitions through which the glass might escape. Of course, there are too many saddle points around a configuration to sample them all, but several thousand saddle-point configurations can be determined with ART from a given configuration, which is enough to obtain statistical distributions. Figure 2(a) shows the probability distributions of activation energies for saddle points around the glassy configurations obtained at the end of the cooling procedures shown in fig. 1(a).

The distributions shown in fig. 2(a) have specific features, shared also by two-dimensional systems [18,17]. First, activation energies form a continuous spectrum,

which is characteristic of complex energy landscapes, as also obtained in amorphous silicon [29]. Second, the energy range of the distributions is large, up to $30\epsilon_{AA}$, with an exponential decay at high energies as shown by the dashed exponential fit in fig. 2(a). The latter decay is consistent with the prediction of a master equation approach proposed by Dyre in ref. [30]. The latter is primarily based on the distribution of IS energies but was extended by first-order expansion to the distribution of activation energies. Third, the distributions have a maximum, *i.e.* a most likely activation energy, which is on the order of $10\epsilon_{AA}$. Note that this maximum slightly increases when the quench rate decreases. Finally, the distributions contain low activation energies, almost down to zero. As seen in fig. 2(a), the density of these low activation energies is directly correlated to the cooling rate: more slowly cooled glasses have less low activation energies than more rapidly cooled glasses.

Figure 2(b) displays the energy difference between initial and final configurations of 1000 transitions as a function of the activation energy of the transition. As the quench rate decreases, the number of transitions with a negative energy difference, *i.e.* transitions that decrease the energy of the glass, decreases. This fact is another signature of the increasing level of relaxation of more slowly quenched glasses. In contrast, for equilibrium MD dynamics the distribution of energy changes is symmetric with exponential tails [31]. Two special cases can be identified in fig. 2(b). Some transitions have almost the same energy difference and activation energy, *i.e.* the final energy is almost the same as the activation energy. Such transitions occur when the final configuration is very close to the activated state with a final energy only slightly below the activation energy. The second limiting case are transitions with zero energy difference, *i.e.* a final energy almost identical to the initial energy. Such transitions occur when two or more atoms replace each other without changing the overall atomic configuration. Figure 2(b) also shows that, for each activation energy, there is a broad spectrum of energy differences. There is therefore no strong correlation between the activation energy of an event and its associated energy difference, as is confirmed by the correlation coefficients noted in the figure. Simple models that link the activation energy of an event to its energy difference between initial and final configurations (for example by adding a fixed energy height to the average of the energy in the initial and final states) [32] can therefore not be applied in glasses.

In the literature, the level of relaxation of glasses has also been related to the local atomic environment and short-to-medium range order in the glass [8,33,22]. Namely, in several binary glasses, including CuZr [34], the smaller species tends to be surrounded by 12 first neighbors that form an icosahedron, in order to achieve efficient local packing. It was shown that the slower the quench rate, the larger the fraction of atoms with an icosahedral environment [34]. To check if the present potential verified this property, we used a Voronoi tessellation [35] to identify the first-neighbor polyhedra for each atom in the glassy configurations obtained above. We found that
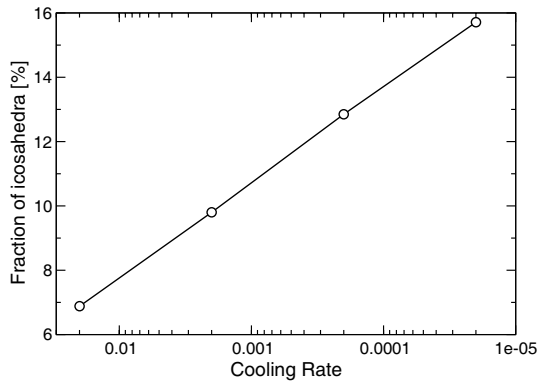
Fig. 3. Fraction of atoms surrounded by a shell of first neighbors that forms an icosahedron as a function of the cooling rate used to obtain the glassy configurations.

indeed, icosahedra are the most frequent polyhedra, as already reported in ref. [21]. Moreover, we observed empirically in fig. 3 that the fraction of atoms surrounded by icosahedra increases logarithmically with the inverse cooling rate. For an analysis of the geometry of the equilibrium dynamics at low temperatures of the model studied here, see ref. [36].

We have identified 3 markers that allow to compare the level of relaxation of quenched glasses: the potential energy of the glass, *i.e.* a thermodynamic marker, the density of low activation energies, *i.e.* a kinetic marker, and the fraction of icosahedron-surrounded atoms, *i.e.* a topological marker. Also, better relaxed glasses are more stable thermodynamically, because they have a lower potential energy, and are more stable kinetically, because they are surrounded by higher activation energies. This property of the PEL was suggested by MD simulations [2] but the present results are the first direct demonstration of the effect.

4 PEL of deformed glasses

The influence of a plastic deformation on the PEL was investigated by deforming the glasses obtained in the previous section in simple shear up to 100% and by using ART on the configurations after deformation to sample locally their PEL. The shear stress/shear strain curves are shown in fig. 1(b). The rapidly cooled glass has a very short elastic regime followed by a steady-state plastic regime, while the most slowly cooled glass has a much longer elastic regime with an upper-yield point followed by softening before entering the steady-state regime. Similar effects have been obtained in other glass formers [37,34]. In the steady-state regime, the potential energy and stress are independent of the initial configuration of the glass. Also, interestingly, the potential energy in the steady state is close to that of the initial liquid, on the left-hand side of fig. 1(a).

The distributions of activation energies in the final configurations after 100% deformation are shown in fig. 4(a). All distributions are now equivalent with a high density
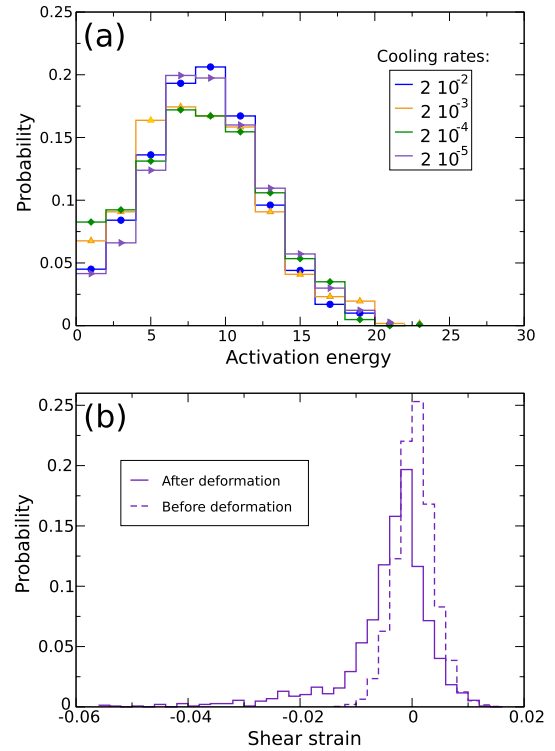
Fig. 4. Influence of a plastic deformation on the PEL of glasses: (a) distribution of activation energies in the glasses obtained at different cooling rates in fig. 1, after 100% shear strain; (b) distribution of inelastic strains in the glass cooled at 2×10^{-5} before (dashed line) and after (solid line) plastic deformation.

of low activation energies. The plastic deformation has thus taken the glasses to high energy/low stability configurations independent of the initial configuration of the glass, a process called *rejuvenation* [38], by opposition to *ageing* that takes the glass into configurations of lower energy/larger stability.

The high-energy configurations visited by the glass during plastic deformation contain a signature of the symmetry of the applied deformation, *i.e.* the configurations are *polarized* [39]. Polarization is most readily seen by computing the distribution of inelastic strains that correspond to each transition, *i.e.* the difference of shear stress between initial and final configurations divided by the shear modulus. The resulting distribution is shown in fig. 4(b) for the most slowly cooled glass before and after plastic deformation. Before plastic deformation, the distribution is symmetrical with respect to zero because there is no bias between positive or negative strains. After deformation, the distribution is asymmetrical and contains more negative than positive events. This asymmetry is specific to the applied shear deformation (which was in the positive direction) and explains straightforwardly the anelastic behavior of glasses. Indeed, glasses are known to undergo a time- and temperature-dependent recovery after plastic deformation, called *anelasticity* [40,39]. This effect is explained by the fact that, upon annealing after shear deformation, the glass undergoes more transitions

with a negative strain than transitions with a positive strain, because of the asymmetry of the strain distribution shown in fig. 4(b). The glass therefore develops a negative deformation, *i.e.* a deformation in the direction opposite to the initial direction of deformation. This effect was checked by activated dynamics on a two-dimensional glass in ref. [17]. It was also shown that after annealing and anelastic recovery, the distribution was again symmetrical around zero strain.

5 PEL of supercooled liquids

MD simulations in the supercooled regime have been extensively used to obtain "inherent dynamics", *i.e.* to track the succession of basins visited by a supercooled liquid during its time evolution, at temperatures near and above T_C [11–13,41–43,4]. In the work of Schrøder *et al.* [11], the succession of transitions was determined for the same binary LJ potential as in previous section, for a system containing 500 particles at a temperature of $T = T_C = 0.59$. The average potential energy per atom of this system (after energy minimization to remove the kinetic part) is about $-6.9\epsilon_{AA}$ and the fraction of icosahedron-surrounded atoms is around 11%. Compared to figs. 2 and 3, these markers place the supercooled liquid in the intermediate range of relaxation. Of course, a quantitative comparison between the quenched glasses of previous sections and the present supercooled liquid is difficult because the present system is much smaller and finite-size effects may be significant. Quenches of the present system at the same rates as in sect. 3 after heating the liquid up to $T = 1.2$ show that $-6.9\epsilon_{AA}$ is the typical energy reached with a quenched rate of $2 \cdot 10^{-4}$, which is consistent with an intermediate level of relaxation.

By refining the frequency of energy minimizations, the initial and final configurations of each transition was determined. Here, the NEB method was used to determine the saddle-point configuration of each MD transitions. Figure 5(a) shows the corresponding activation energy probability. ART was also used to determine the spectrum of activation energies from a given configuration representative of the configurations visited by the system during the MD simulation. The corresponding activation energy probability is shown in fig. 5(b). Activation energies are shifted to higher energies compared to fig. 2(a), and the distribution appears more symmetrical and is well fitted by a Gaussian distribution. We checked on quenched glasses made of 500 atoms that this difference is mainly a finite-size effect and that the distribution shown in fig. 5(b) is similar to that of a glass quenched with an intermediate quench rate.

The difference between the distributions in figs. 5(a) and (b) arises from the fact that in the MD simulation, the occurrence of a given activation energy is weighted by its Boltzmann factor. More precisely, the MD distribution in fig. 5(a) should be proportional to the weighted distribution $\rho(E)\exp(-E/k_BT)$, where $\rho(E)$ is the distribution from ART and $T = 0.59$. The dashed curve in fig. 5(a) is the resulting weighted distribution, which agrees well
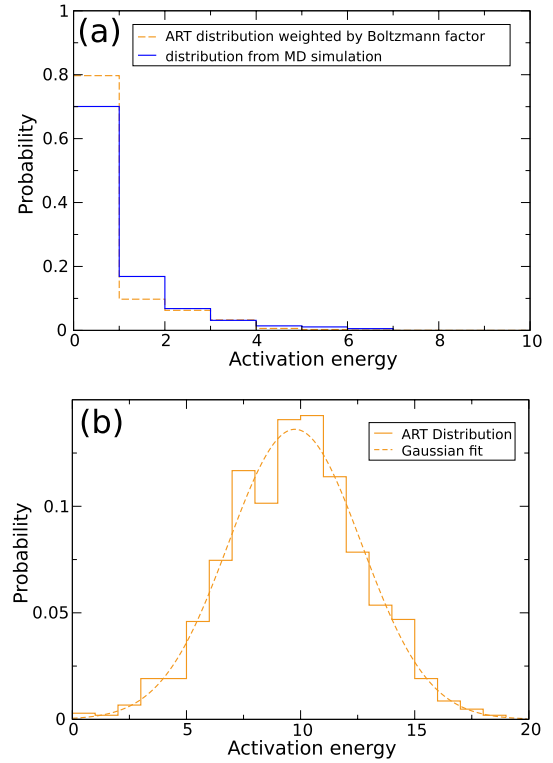
Fig. 5. Distribution of activation energies: (a) the distribution is computed from the succession of transitions undergone during a MD simulation at $T_C = 0.59$; (b) the distribution is computed from an ART sampling on a configuration of the same system as in (a). In (a), the dashed distribution is the ART distribution weighted by Boltzmann factor.

with the MD distribution. We should note, however, that this distribution involves only the lowest activation barriers of the ART distribution. The larger activation energy transitions, which are much more abundant, do not appear in fig. 5(a) due to their negligibly small Boltzmann factor.

To further compare the transitions found by MD and by ART, we computed for 1000 transitions found with each method four well-known measures shown in fig. 6. The first measure is the mean-square displacement of each transition, defined as

$$\delta^2 = \frac{1}{N}\sqrt{\sum_{i=1}^{N}|\mathbf{r}_i^F - \mathbf{r}_i^I|^2}, \qquad (1)$$

where $\mathbf{r}_i^I$ and $\mathbf{r}_i^F$ denote the position of atom i in the initial and final configurations of the transition, respectively. The second measure is the fraction of mobile (or "active") particles, defined as the fraction of particles that move by more than $0.2\sigma_{AA}$ [11]. The third measure is the number of broken bonds, obtained as the number of first-neighbor bonds broken during the transitions. The fourth measure is the participation ratio of each transition, defined as

$$r = \frac{1}{N}\frac{\left(\sum_{i=1}^{N}|\mathbf{r}_i^F - \mathbf{r}_i^I|^2\right)^2}{\sum_{i=1}^{N}|\mathbf{r}_i^F - \mathbf{r}_i^I|^4}. \qquad (2)$$
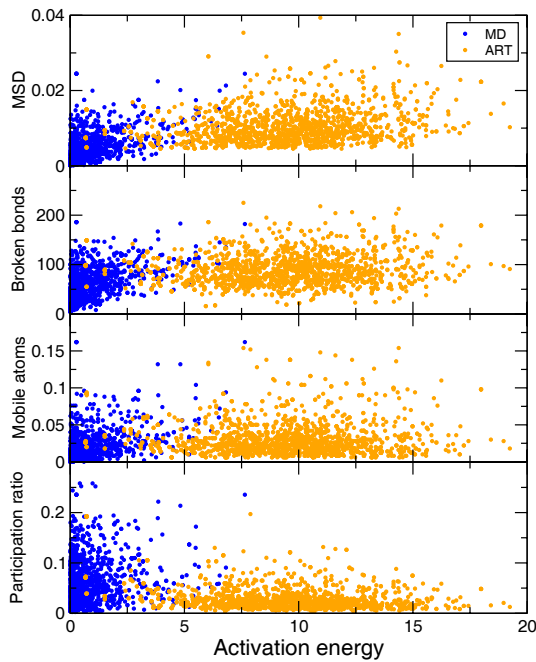
Fig. 6. Scatter plot of geometrical factors characterizing thermally activated events found either by MD or by ART and shown as a function of their activation energy. From top to bottom are shown the mean-square displacement, the number of first-neighbor broken bonds, the fraction of mobile atoms, the participation ratio. In all cases, 1000 transitions are shown for both methods.

As shown in fig. 6, the energy ranges visited by MD and ART are almost disjoined. One reason is the suppression of high activation energy transitions in the MD simulation because of their negligibly small Boltzmann factor. Another reason is the apparent inability of ART to find very low activation barriers, which may depend on the choice of parameters used in ART (mainly the choices of step lengths, curvature threshold and number of atoms involved in the initial direction of motion). From fig. 6, we also see that in the region of higher activation energies sampled by ART, the mean-square displacement and number of broken bonds are larger than in the lower activation energy region sampled by MD. By contrast, the number of mobile particles appears mostly uncorrelated with the activation energy and similar with both methods. Finally, the transitions found by ART appear more localized than those found by MD, as evidenced by the smaller participation ratio of ART transitions compared to MD transitions.

We have seen that if we restrict the ART distribution to its lowest activation energies, there is a good agreement between MD and ART, although we should note that the distribution in fig. 6 is mainly controlled by the exponential decay of the Boltzmann factor. ART finds higher activation energy transitions with larger mean-square displacements and more broken bonds than the transitions found in MD. One possible explanation is that MD finds mainly transitions inside a given metabasin while ART is biased towards transitions between metabasins that are

known to involve larger mean-square displacements and more broken bonds [44,45]. The above observations are only preliminary results that should be confirmed by simulations in larger systems to avoid finite-size effects and using MD in a larger temperature range, extending below T_C, in order to access the true thermally activated regime.

6 Conclusion

ART is an efficient algorithm to sample the configuration space of complex systems, such as glasses. It can be used for 3D systems containing a substantial number of atoms. The calculations performed here show that the local PEL around glassy and supercooled configurations contain signatures of the history of the system and its level of relaxation, which is directly correlated to the density of low activation energies. Also the polarization of the configuration, seen in the distribution of inelastic strains, is an important aspect of glass deformation. Accounting for polarization in a mean-field description of the glass microstructure cannot be achieved by a scalar variable, such as the free volume, but will require a tensorial internal variable. Finally, the fact that ART mainly finds transitions between metabasins is an interesting feature that can be used to perform kinetic Monte Carlo simulations. Indeed, MD simulations have shown that glasses undergo a Brownian motion between metabasins [41] and therefore the distributions obtained from ART would be appropriate for a kinetic Monte Carlo sampling in order to simulate the evolution of a glass over experimental timescales retaining atomistic fidelity.

References

1. M.D. Ediger, C.A. Angell, S.R. Nagel, J. Chem. Phys. **100**, 13200 (1996).
2. P.G. Debenedetti, F.H. Stillinger, Nature **410**, 259 (2001).
3. G. Tarjus, S.A. Kivelson, Z. Nussinov, P. Viot, J. Phys.: Condens. Matter **17**, R1143 (2005).
4. A. Heuer, J. Phys.: Condens. Matter **20**, 373101 (2008).
5. H. Tanaka, T. Kawasaki, H. Shintani, K. Watanabe, Nat. Mater. **9**, 324 (2010).
6. L. Berthier, G. Biroli, Rev. Mod. Phys. **83**, 587 (2011).
7. F.H. Stillinger, T.A. Weber, Science **225**, 983 (1984).
8. H. Jónsson, H.C. Andersen, Phys. Rev. Lett. **60**, 2295 (1988).
9. F.H. Stillinger, Science **267**, 1935 (1995).
10. S. Sastry, P.G. Debenedetti, F.H. Stillinger, Nature **393**, 554 (1998).
11. T.B. Schroder, S. Sastry, J.C. Dyre, S.C. Glotzer, J. Chem. Phys. **112**, 9834 (2000).
12. S. Büchner, A. Heuer, Phys. Rev. Lett. **84**, 2168 (2000).
13. B. Doliwa, A. Heuer, Phys. Rev. Lett. **91**, 235501 (2003).
14. D.J. Wales, M.A. Miller, T.R. Walsh, Nature **394**, 758 (1998).

15. R. Malek, N. Mousseau, Phys. Rev. E **62**, 7723 (2000).
16. E. Cancès, F. Legoll, M.C. Marinica, K. Minoukadeh, F. Willaime, J. Chem. Phys. **130**, 114711 (2009).
17. D. Rodney, C.A. Schuh, Phys. Rev. B **80**, 184203 (2009).
18. D. Rodney, C. Schuh, Phys. Rev. Lett. **102**, 235503 (2009).
19. G. Wahnström, Phys. Rev. A **44**, 3752 (1991).
20. Y. Shi, M.L. Falk, Phys. Rev. B **73**, 214201 (2006).
21. D. Coslovich, G. Pastore, J. Chem. Phys. **127**, 124504 (2007).
22. K. Watanabe, H. Tanaka, Phys. Rev. Lett. **100**, 158002 (2008).
23. D. Rodney, M. Fivel, R. Dendievel, Phys. Rev. Lett. **95**, 95108004 (2005).
24. H. Jónsson, G. Mills, K. Jacobsen, in *Classical and Quantum Dynamics in Condensed Phase Simulations*, edited by B.J. Berne, G. Ciccotti, D.F. Coker (World Scientific, Singapore, 1998) p. 385.
25. D. Rodney, Phys. Rev. B **76**, 144108 (2007).
26. G. Henkelman, H. Jónsson, J. Chem. Phys. **113**, 9978 (2000).
27. G. Henkelman, B.P. Uberuaga, H. Jónsson, J. Chem. Phys. **113**, 9901 (2000).
28. M. Goldstein, J. Chem. Phys. **51**, 3728 (1969).
29. F. Valiquette, N. Mousseau, Phys. Rev. B **68**, 125209 (2003).
30. J.C. Dyre, Phys. Rev. Lett. **58**, 792 (1987).
31. N.P. Bailey, T.B. Schrøder, J.C. Dyre, Phys. Rev. Lett. **102**, 055701 (2009).
32. E.R. Homer, D. Rodney, C.A. Schuh, Phys. Rev. E **81**, 064204 (2010).
33. H.W. Sheng, W.K. Luo, F.M. Alamgir, J.M. Bai, E. Ma, Nature **439**, 419 (2006).
34. Y.Q. Cheng, A.J. Cao, E. Ma, Acta Mater. **57**, 3253 (2009).
35. C.H. Rycroft, G.S. Grest, J.W. Landry, M.Z. Bazant, Phys. Rev. E **74**, 021306 (2006).
36. U.R. Pedersen, T.B. Schrøder, J.C. Dyre, P. Harrowell, Phys. Rev. Lett. **104**, 105701 (2010).
37. Y. Shi, M.L. Falk, Phys. Rev. Lett. **95**, 095502 (2005).
38. M. Utz, P. Debenedetti, F.H. Stillinger, Phys. Rev. Lett. **84**, 1471 (2000).
39. A.S. Argon, H.Y. Kuo, J. Non-Cryst. Solids **37**, 241 (1980).
40. A.S. Argon, J. Appl. Phys. **39**, 4080 (1968).
41. B. Doliwa, A. Heuer, Phys. Rev. E **67**, 030501 (2003).
42. B. Doliwa, A. Heuer, Phys. Rev. E **67**, 031506 (2003).
43. R.A. Denny, D.R. Reichman, J.P. Bouchaud, Phys. Rev. Lett. **90**, 025503 (2003).
44. T.F. Middleton, D.J. Wales, Phys. Rev. B **64**, 024205 (2001).
45. G.A. Appignanesi, J.A. Rodriguez Fris, R.A. Montani, W. Kob, Phys. Rev. Lett. **96**, 057801 (2006).